Coupling pore network and finite element methods for rapid modelling of deformation

Samuel Fagbemi¹ and Pejman Tahmasebi^{1,2,†}

¹Department of Petroleum Engineering, University of Wyoming, Laramie, WY 82071, USA ²Department of Civil Engineering, University of Wyoming, Laramie, WY 82071, USA

(Received 21 June 2019; revised 6 November 2019; accepted 4 May 2020)

Numerical modelling of deformation in hydromechanical systems can be timeconsuming using fully coupled classical numerical methods for large representative porous media samples. In this paper, we present a new two-way coupled partitioned fluid-solid system. The coupled system is applied for simulating geomechanical processes at the pore-scale. We track the deformation of the solid resulting from the drainage of resident fluids in the pores, as well as the evolution of fluid properties from dynamic loading. The finite element method is responsible for capturing the structural deformation in the coupled system while the dynamic pore network is used for modelling multiphase flow in the fluid subsystem. A fictitious fluid-solid interface is created at each pore network-finite element node junction via convex hulling, followed by data exchange using linear interpolation. The results show good agreement with a pre-existing coupled finite volume model and the computations are completed in much less time.

Key words: flow-structure interactions, granular media, porous media

1. Introduction

The movement of fluids in porous media has been widely studied in various fields. A porous medium initially saturated with a fluid can undergo implosive collapse due to a change in pore pressure (Bueno & Gomez 2016; Alvarez 2017). An alteration in fluid properties at a large scale could lead to creep formation (Zhu, He & Yin 2014). In addition, polyaxial stresses acting on a porous medium in the presence of pore fluids can induce significant deformation. Such occurrences may significantly alter the hydromechanical equilibrium of the porous media, especially in samples with low-to-medium compressive strength. It has been shown that stress application has a controlling influence on pore-size distribution, porosity, tortuosity, absolute permeability, relative permeabilities and capillary pressure (Zhu & Wong 1996). Therefore, it is clear that the hydromechanical interactions between the fluids located in pore spaces and adjacent structures need to be accounted for. Models for interactions between fluids and solids should be coupled within a robust

framework (Zienkiewicz, Taylor & Taylor 2000; Zhang & Tahmasebi 2018; Tahmasebi & Kamrava 2019).

In the literature, the traditional approach for achieving fluid–solid coupling is referred to as fluid–structure interaction (FSI). A joint finite element methodology is typically used to solve equations for both fluids and solids, along with the deforming interface (Bathe, Zhang & Ji 1999; Rugonyi & Bathe 2001; Bathe & Zhang 2004; Vierendeels *et al.* 2007; Sathe & Tezduyar 2008). Another technique that has gained significant recognition is the hybrid technique of employing finite volume (FV) for the fluid domain and finite element (FE) for the solid. This technique takes advantage of the strength of both solvers, given that FE is conventionally applied to solving computational solid mechanics equations while FV is used for computational fluid dynamics (known as CFD) problems (Campbell 2010; Munsch & Breuer 2010). Other techniques include lattice Boltzmann method finite element (known as LBM*-FE) (Kollmannsberger *et al.* 2009; Geller *et al.* 2010) and discrete element method (known as LBM*-DEM) (Han & Cundall 2012); the asterisk denotes flow solvers.

Coupled methods can be classified as either monolithic or partitioned. In the monolithic approach, the governing equations are solved within the same computational framework; in the partitioned approach, both equations are solved separately and then coupled via coupling algorithms. The latter is less memory intensive and easier to implement. However, some aspects such as code-to-code communication or grid-to-grid interpolation (e.g. of loads and displacements) must be considered. The monolithic approach, on the other hand, requires a multidisciplinary approach in which communication between both solvers occurs synchronously within the same code. The solutions tend to be more accurate than those generated by the partitioned approach; however, they can be very memory intensive, and it may be difficult to manage the codes. This paper, therefore, focuses only on the partitioned method.

Some of the difficulties encountered in coupled fluid–solid solver applications are that the partial differential equations are always nonlinear in nature, and analytical equations often do not exist to validate the results. Some data have been made available for numerical benchmarking of problems involving elastic deforming structures in the presence of laminar incompressible flow (Turek & Hron 2006; Turek et al. 2010), as well as experimental data (Gomes & Lienhart 2006). Nevertheless, the time-consuming nature of the simulations, especially for porous media applications (as shown in table 1), remains a major problem. For example, the physical time required to directly solve for two-phase flow alone, through a segmented 120^3 voxels sandstone rock geometry, of porosity $23\,\%$ and $502\,$ k cells, is approximately nine hours or more depending on the application. For a coupled system of the same geometry, it takes nearly 5×9 hrs, even with a supercomputer cluster of 200 cores. Consequently, in this study we attempt to improve computational efficiency by applying a meshless technique for the fluid while still maintaining a boundary-fitted technique for the solid, to ensure optimal accuracy for the coupled model.

Direct simulation methods for fluid solvers tend to be time-consuming, especially for multiphase fluid simulation (Joekar-Niasar & Hassanizadeh 2012). In general, the pore network (PN) method (Fatt 1956) is an efficient alternative for modelling porescale processes, using ideal geometries. The entire porous medium is represented as a network of nodes (pore bodies) and connecting channels (throats) comprising circular and triangular cross-sections, as well as other descriptive elements. This technique has been adopted for a wide range of applications, including two-phase flow (Bryant & Blunt 1992; Blunt 1995; Oren, Bakke & Arntzen 1998), foam injection (Kharabaf & Yortsos 1998; Chen, Yortsos & Rossen 2005), drying processes (Figus *et al.* 1999),

Method	Fluid		Coupled			Decoupled		
	Cells ×10 ³	CPU time (min)	Fluid cells × 10 ³	Solid cells ×10 ³	CPU time (min)	Fluid cells × 10 ³	Solid cells ×10 ³	CPU time (min)
FV-FV*	502.7	508.76	466.8	1493.5	2797.2			
FE-FE*	218.7	389.68	_	_	_	_	_	_
FE-FV*	_	_	_	_	_	502.7	827.9	626.7
FE-DPN*	640ª	2	640	56.5	186.9	640	56.5	10.6

TABLE 1. Comparison of the computational times for various coupled pore-scale solvers on a domain with 120³ voxels. Note that the review of speeds of coupled solvers includes the preliminary results of this work. Similar step size and different cell sizes were used. Coupled and decoupled solutions were performed using multiphase fluids, while the stand-alone fluid simulations were performed for both multiphase (with FV) and single-phase flow (with FE). The central processing unit, CPU, time is reported in minutes. The FE-DPN*, which is the method implemented in this work, came out fastest by far in all categories; DPN represents dynamic pore network.

^aNumber of nodes and throats.

Note: The cells indicated for the DPN* are the number of pore bodies and throats divided by 1000.

contaminant transport (Bijeljic & Blunt 2007) and three-phase flow (Pereira *et al.* 1996). Although PN far surpasses other flow solvers in terms of speed, its accuracy has often been questioned because it simplifies the pore-space geometry. This idealization could lead to loss of geometric and topological information. However, some models have been shown to yield an acceptable match with experimental values for relative permeability and capillary-saturation curves (Oren *et al.* 1998).

In this work, we develop a new segregated coupled pore-scale solver in which DPN (a variation of PN) is used for simulating multiphase fluid flow, while FE is used for solving the solid equations. The use of DPN can be a valuable tool in coupled pore-scale modelling, as it can be quite fast and can potentially be applied to larger domains. Here, DPN is used for modelling the fluid system based on prescribed inlet flow rate boundary conditions. The solid is assumed to experience large deformations; therefore, it is modelled as a nonlinear elastic material. A fictitious fluid–solid interface is created at the DPN-finite element node junction via convex hulling, followed by data exchange using linear interpolation.

The rest of this paper is arranged as follows: the first section examines the equations of the fluid and solid solvers, including the coupling methodology; the next section examines the application for an elastically deforming rock matrix experiencing drainage in a water-wet system. We then verify the model with respect to an FV model.

2. Methodology

We study the response of an elastic porous medium interacting with immiscible and incompressible fluids. We focus on three-dimensional geometries while considering large displacements of the rock matrix. The fluid motion is modelled using DPN and the solid deformation is modelled using the FE methodology. The fluid in the network interacts with the solid matrix, inducing elastic deformation; and this deformation

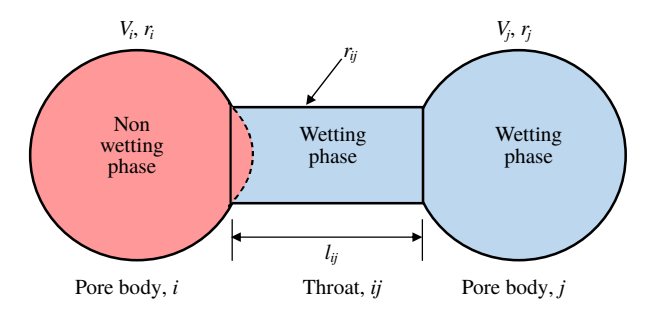


FIGURE 1. A local PN structure.

leads to changes in pore pressure, thus giving rise to two-way hydromechanical coupling. We neglect the effect of gravitational forces in this work because of the scale of investigation. Both models are coupled using a segregated or partitioned approach and linked together via a fictitious boundary.

2.1. DPN flow model

In DPN, the spatial arrangements of pores and throats are obtained, directly from segmented images. In this work, this was achieved using the maximal ball method (Dong & Blunt 2009), which can perform direct mapping of the actual sample to an irregular lattice. We calculated the pore body volumes and throat conductances based on the void space geometry. The pores are commonly represented in cubic or spherical form. For pore throats, however, a variety of geometric shapes with various cross-sections such as stars, circles, triangles, squares, etc., could be used. In this work, we use spherical pore bodies and cylindrical throats. Figures 1 and 2 show a typical arrangement of a network, with pore bodies (nodes) indicated by indices i and i, and throats l_{ii} connecting both nodes i and j. Depending on the driving mechanism, PN can be implemented either quasi-statically or dynamically. In quasi-static PN modelling, invasion of the pores is based solely on capillary entry pressure. Capillary pressure is imposed through boundary conditions on the network lattice. The position of fluid-fluid interfaces is then determined at each stage of the fluid displacement process independent of the time of the simulation, then the simulation runs until an equilibrium is attained between the prescribed capillary pressure and that of the system. If the interface is unstable, it moves through the network until a stable position is found or until it reaches the outlet. No time dependence is included in the calculation and the interface simply moves from one equilibrium position to another (Celia, Reeves & Ferrand 1995). Quasi-static models can be considered extensions of simple percolation models, with drainage floods being modelled through invasion percolation and imbibition through adapted bond percolation processes (Li, Mcdougall & Sorbie 2017).

Quasi-static systems are not time dependent and are, consequently, unsuitable for the problem at hand due to the transient nature of the coupled system whose fluid and structural properties must evolve with time. Therefore, we employ a dynamic approach. In DPN systems, the model solves the pressure evolution problem based on capillary entry pressure and introduces a time dependent pore-filling mechanism. The emergent rate-dependent flow regimes are determined by a competition between capillary and viscous forces. The DPN model calculates the pressure forces by solving pressure evolution based on minimum filling time for each of the pores, which are eventually

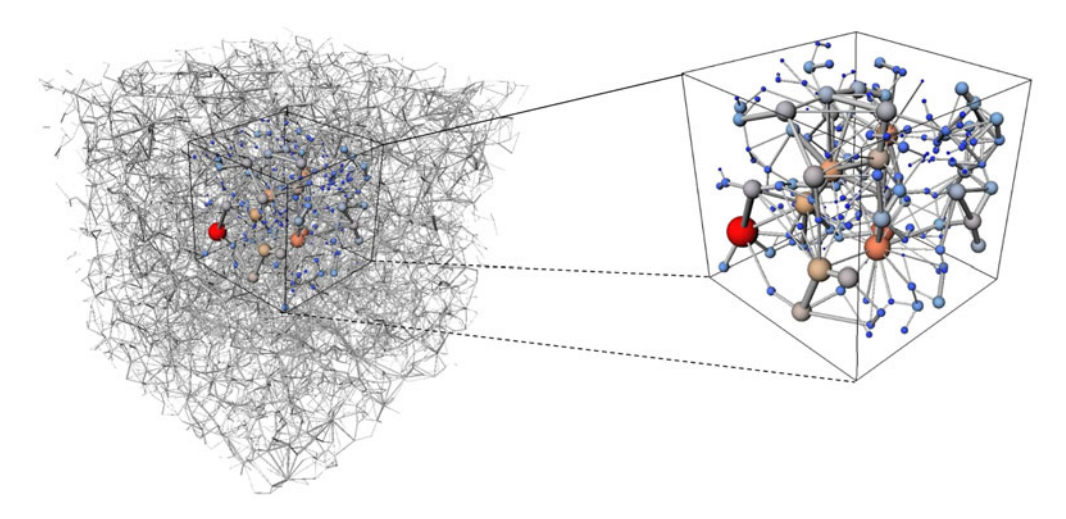


FIGURE 2. A subsample or elementary volume used for coupling simulations.

imparted onto the solid phase. If the pores are located in domain Ω_f , and fluid flow in the pore throats is laminar, given Poiseuille's law, each fluid phase obeys the following volume conservation law:

$$V_i \frac{\partial S_i}{\partial t} + \sum_{i \in N} Q_{ij} = 0, \quad \text{in } \Omega_f$$
 (2.1)

where N is the number of pore bodies, V_i is the volume of pore body i, S_i represents the local saturation of the reference phase and Q_{ij} is the total volumetric flux from pore body i to pore body j. If a channel or throat is completely filled with a single fluid, the flow rate along the throat from pore body i to pore body j can be calculated by

$$Q_{ij} = G_{ij}(\Phi_i - \Phi_j), \qquad (2.2)$$

where Φ_k is the hydraulic potential in pore body $k = \{i, j\}$ defined as $P_k + \rho g h_k$, where h_k is the coordinate of the pore k in the direction of the gravitational field, P_k is the fluid pressure in pore k, g is the gravitational force and G_{ij} is the throat conductance, defined as

$$G_{ij} = \frac{S_{\alpha} r_{ij}^4}{l_{ij} \eta},\tag{2.3}$$

where S_{α} is the shape factor, r_{ij} is the radius of the connecting throat, l_{ij} is the length of the throat taken from the centroids of pore body i and pore body j, and η is the fluid viscosity. The conductance is calculated at every throat location and is dependent on its radius and length. By applying a pressure gradient across the network (via boundary conditions), the pressure field inside the network can eventually be obtained by applying mass conservation at each interior node i,

$$\sum_{i \in N_i} Q_{ij} = 0. \tag{2.4}$$

For more than one fluid occupying the throat, the effects of capillary pressure must be accounted for across the fluid-fluid interface. The DPN model can be further simplified by using a circular throat cross-section, which prevents corner flow. For the case of drainage, if the displacement occurs in a piston-like manner and the effects of gravity are neglected, equation (2.2) is rewritten as

$$Q_{ij} = G_{ij}(P_i - P_j - \Delta P_{ij}^c), (2.5)$$

where

$$G_{ij} = S_{\alpha} r_{ij}^{4} \left(\frac{1}{l_{ij}^{(i)} \eta_{i}} + \frac{1}{l_{ij}^{(j)} \eta_{j}} \right). \tag{2.6}$$

In equation (2.6), η_i and η_j are the viscosities of the fluids in segments of the pore throats adjacent to pore i and pore j, while $l_{ij}^{(i)}$ and $l_{ij}^{(j)}$ are the corresponding segment lengths. The capillary pressure jump between the fluid–fluid interface is expressed by the Young–Laplace equation,

$$\Delta P_{ij}^c = \gamma_{sf} \cos \theta \left(\frac{1}{R_1} + \frac{1}{R_2} \right), \tag{2.7}$$

where R_1 and R_2 are the radii of curvature of the interface in any two orthogonal planes, θ is the contact angle and γ_{sf} is the surface tension. For a given distribution of fluids, the phase conductances are calculated from (2.6). The pressure fields can be computed by substituting (2.5) into (2.4), which yields the following linear system of equations:

$$[G]{P} = [B], \tag{2.8}$$

where G is the matrix of the conductivities, P is the vector of unknown nodal pressures and B is a vector formed from boundary pressures and capillary pressures. This equation can be solved using the biconjugate gradient solution method. The updated pressure field is then used in (2.5) to compute fluxes through the pore throats. Simulations can also be carried out with constant injection rate boundary conditions (Aker *et al.* 1998), which we used in this work. After solving for the volumetric fluxes of all capillary elements, the current invading phase saturation in each pore body is used to determine the minimum filling time for each of the pores; this is set as the time step size Δt . This time step corresponds to the shortest time required to fill one non-wetting phase-filled pore. Then, equation (2.1) is used to update the saturation in each pore body.

2.2. Finite element method

In this paper, the solid response is quantified using finite element formulation. We assume that the solid undergoes large deformations and, as such, we model the solid domain as nonlinear elastic. For a spatial solid domain $\Omega_s^0 \subset \mathbb{R}^d$ bounded by Γ , the continuum equations can be described in total Lagrangian form as

$$\rho_0 \ddot{\boldsymbol{u}} = \nabla_0 \cdot (\boldsymbol{S} \cdot \boldsymbol{F}^{\mathrm{T}}) + \rho_0 \boldsymbol{b} \quad \text{in } \Omega_s^0, \tag{2.9a}$$

$$u = \overline{\overline{u}} \quad \text{on } \Gamma_D^0,$$
 (2.9b)

$$(\mathbf{S} \cdot \mathbf{F}^{\mathrm{T}}) \cdot \mathbf{n} = \overline{\overline{\mathbf{T}}} \quad \text{on } \Gamma_{N}^{0}, \tag{2.9c}$$

where 0 indicates the quantities related to the initial (undeformed) configuration, the displacement of the solid phase is denoted by u, while each dotted accent represents

the time derivative and F is the deformation gradient, $F = \nabla_0 u$. The Dirichlet and Neumann partitions at the boundaries are u and \overline{T} , respectively. Here, n is the unit surface normal in the reference configuration, ρ_0 is the initial density and b is the body force per unit mass. The stress is obtained in terms of the second Piola–Kirchoff stress tensor S and the Green strain tensor E. The first Piola–Kirchoff stress is related to S by $P = S \cdot F^T$. For a finite element discretization, $B_{oh} = \bigcup_{e=1}^{E} \Omega_s^{e,*}$ which is a combination of Ω_0^e and $\Gamma_0^e = \Gamma_D^0 \cup \Gamma_N^0$. The finite-dimensional piecewise polynomial approximation u_h , P_h of the solution is defined in the spaces

$$X_{h}^{k} = \{ \boldsymbol{u}_{h} \in L^{2}(B_{oh}) | [\boldsymbol{u}_{h}|_{\Omega_{0}^{e}} \in \mathbb{M}^{k}(\Omega_{0}^{e}) \forall \Omega_{0}^{e} \in B_{oh}] \} \subset X^{f}(B_{oh}) = \prod_{e} (H^{1}(\Omega_{0}^{e})), \quad (2.10)$$

$$S_h^k = \{ \mathbf{P}_h \in [L^2(B_{oh})]^2 | [\mathbf{P}_h|_{\Omega_0^e} \in \mathbb{M}^k(\Omega_0^e)^2 \forall \Omega_0^e \in B_{oh}] \} \subset S^f(B_{oh}) = \prod_e (H^1(\Omega_0^e))^2, \quad (2.11)$$

where \mathbb{M}^k is the set of polynomial functions up to degree $k \ge 1$. Let δu_h be an arbitrary test function defined in the space

$$X_{hc}^{k} = \{\delta \boldsymbol{u}_{h} \in X_{h}^{k} | [\delta \boldsymbol{u}_{h} = 0 \forall X \in \partial B_{oh}, \forall t \in T \text{ and } \delta \boldsymbol{u}_{h}(t_{0}) = 0 \forall X \in B_{oh} \delta \boldsymbol{u}_{h}(t_{f}) = 0 \forall X \in B_{oh} \} .$$

$$(2.12)$$

The weak formulation of the expression is carried out by integration in the reference coordinate system by finding $u_h \in X_h^k$ and $P_h \in S_h^k$, such that

$$\sum_{e} \int_{\Omega_{0}^{e}} (\rho_{0} \ddot{\boldsymbol{u}}_{h} - \nabla_{0} \cdot \boldsymbol{P}_{h}) \cdot \delta \boldsymbol{u}_{h} \, dV = \sum_{e} \int_{\partial \Omega_{0}^{e}} \overline{T} \cdot \delta \boldsymbol{u}_{h} \, dS + \sum_{e} \int_{\Omega_{0}^{e}} \rho_{0} \boldsymbol{b} \cdot \delta \boldsymbol{u}_{h} \, dV \forall \delta \boldsymbol{u}_{h}$$

$$\in X_{hc}^{k}, \, \forall t \in T.$$

$$(2.13)$$

Based on the nonlinear dynamic behaviour of the solid, the following discrete nonlinear system of linear equations can be obtained:

$$\mathbf{M}\ddot{\mathbf{u}}(t) + \mathbf{C}\dot{\mathbf{u}}(t) + \mathbf{f}_{int}(t) = \mathbf{f}_{ext}(t), \tag{2.14}$$

where \mathbf{M} is the $3N \times 3N$ mass matrix, \mathbf{C} is the damping matrix, $\mathbf{f}_{int}(t)$ and $\mathbf{f}_{ext}(t)$ are the internal force vector and the external force vector from the fluid in 3N dimensions, respectively. Since the solution is solved using Lagrangian meshes, \mathbf{M} is time invariant. Vibration effects are not considered in this work, so the damping coefficient is zero. The mass matrix, internal and external forces follow as

$$\mathbf{M}_{IJ} = \int_{\Omega_r} \rho_0 N_I N_J \, \mathrm{d}V, \tag{2.15}$$

$$(\mathbf{f}_{int,I})^{\mathrm{T}} = \int_{\Omega_s} \frac{\partial N_I}{\partial \mathbf{X}} \mathbf{S} \cdot \mathbf{F}^{\mathrm{T}} \, \mathrm{d}V,$$
 (2.16)

$$f_{ext,I} = \int_{\Omega_s} \rho_0 \boldsymbol{b} N_I \, dV + \int_{\Gamma_N^0} \overline{\overline{\boldsymbol{T}}} \cdot N_I \, dS, \qquad (2.17)$$

where N_I is the shape function corresponding to node I. The internal and external nodal forces are functions of nodal displacement and time. The external loads are prescribed as a function of time incrementally. Therefore, assembling the fluid load requires the computation of the time-varying force exerted by the encompassing fluid on the solid across the interface.

2.2.1. Time discontinuous Galerkin method

To solve for the solid response, we apply the time-discontinuous Galerkin method (TDG) (Mancuso & Ubertini 2003; Noels & Radovitzky 2008). A similar procedure has been used by De Rosis *et al.* (2014) for finite element method (FEM) coupling with the lattice Boltzmann method (LBM). However, their coupling methodology was applied only for linear dynamics. The TDG they applied can be easily adapted for nonlinear analysis, such as for Eulerian formulation (for example, see Denoël & Detournay (2011)). The TDG method considered in this work uses piecewise linear time interpolation. It is based on prediction and correction schemes, which can provide the requisite accuracy in a few iterations. The implementation is based on the Nørsett algorithm, which is optimal from the computational standpoint among higher-order unconditionally stable methods (Mancuso & Ubertini 2002).

The integration is accomplished through the incremental solution procedure, in which the time interval of interest (T) is discretized into n^f time steps such that $T = \bigcup_{n=0}^{n=n^f-1} [t^n, t^{n+1}]$ and $\Delta t = t^{n+1} - t^n$ is the time step. The scheme treats the displacement and velocity vectors as independent variables and uses piecewise linear time interpolants. The iterative scheme is summarized by the following equation:

$$\mathbf{M}^* \overline{\mathbf{v}}_k^{l+1}(t) = \mathbf{F}_k(t) - \frac{\partial \mathbf{f}_{int}}{\partial \mathbf{u}} \widetilde{\mathbf{u}}_k^{l+1}(t),
\overline{\mathbf{u}}_k^{l+1}(t) = \widetilde{\mathbf{v}}_k^{l+1}(t) + \mu \Delta t \overline{\mathbf{v}}_k^{l+1}(t),$$
(2.18)

where $\partial f_{int}/\partial u = K^{int}$ is the Jacobian matrix of the internal forces or the tangent stiffness matrix, and the barred terms represent time derivatives. The predictor displacements \tilde{u}_k and velocities \tilde{v}_k are given as

$$\tilde{\boldsymbol{v}}_0^{l+1} = \boldsymbol{v}_*^t + \lambda^* \Delta t (\overline{\boldsymbol{v}}_0^l - \overline{\boldsymbol{v}}_1^l), \tag{2.19a}$$

$$\tilde{\boldsymbol{u}}_0^{l+1} = \boldsymbol{u}_*^t + \lambda^* \Delta t (\overline{\boldsymbol{u}}_0^l - \overline{\boldsymbol{u}}_1^l) + \alpha^* \Delta t \tilde{\boldsymbol{v}}_0^{l+1}, \tag{2.19b}$$

$$\tilde{\boldsymbol{v}}_1^{l+1} = \boldsymbol{v}_*^t + (1 - \alpha^*) \Delta t \overline{\boldsymbol{v}}_0^{l+1}, \tag{2.19c}$$

$$\tilde{\boldsymbol{u}}_{1}^{l+1} = \boldsymbol{u}_{*}^{t} + (1 - \alpha^{*}) \Delta t \overline{\boldsymbol{u}}_{0}^{l+1} + \alpha^{*} \Delta t \tilde{\boldsymbol{v}}_{1}^{l+1}, \tag{2.19d}$$

where u_*^t and v_*^t are the vector of unknown displacements and its time derivative at time t of the FE solution. Here, M^* is the effective mass matrix given by

$$\mathbf{M}^* = \mathbf{M} + \alpha^{*2} \Delta t^2 \frac{\partial \mathbf{f}_{int}}{\partial \mathbf{u}}.$$
 (2.20)

It should be noted that this effective mass matrix is equally symmetric and positive-definite, just as M and K^{int} . The effective load F_k (in which the fluid loads would be transmitted) is obtained within two iterations. Based on the on left Radau abscissas, the effective loads are defined as

$$F_0 = \left(\frac{3\sqrt{2}}{4} - \frac{1}{2}\right) f_{ext,0} + (6 - 3\sqrt{2}) f_{ext,2/3},\tag{2.21}$$

$$F_1 = \frac{3}{2} f_{ext,2/3} - \frac{1}{2} f_{ext,0}, \tag{2.22}$$

where $f_{ext,0}$ is the value of f_{ext} at time t and $f_{ext,2/3}$ is the value at time $t+2/3\Delta t$. Coefficients λ^* and α^* are given as follows:

$$\lambda^* = \sqrt{2} - \frac{4}{3}, \quad \alpha^* = 1 - \frac{\sqrt{2}}{2}.$$
 (2.23*a*,*b*)

The model is iterated twice to achieve third-order accuracy. To complete the TDG algorithm, the following equations are solved at the end of the current time step:

$$\boldsymbol{v}_{\star}^{n+1} = \overline{\boldsymbol{u}}_{1}^{l}, \quad \boldsymbol{u}_{\star}^{n+1} = \boldsymbol{u}_{\star}^{n} + \Delta t [(1 - \alpha^{*}) \overline{\boldsymbol{u}}_{0}^{l} + \alpha^{*} \overline{\boldsymbol{u}}_{1}^{l}]. \tag{2.24a,b}$$

2.3. Coupled model

As stated previously, this work aims to develop a three-dimensional fluid-solid model incorporating FE and DPN. Both solution domains are illustrated in figure 3. Pore fluids exert forces on the solid walls, resulting in deformation and eventual modification of force balance. Additionally, the deformation of the solid results in the rearrangement of its structure which can alter fluid properties and the network topology. Thus, the need to update the network regularly during the simulation to track the deformation of the solid. To achieve the solution of such a system, the fluidic and structural computations are performed sequentially. Therefore, at each time step, we began by solving the DPN equation, from which we obtain the pressure at each node and throat. The DPN solver then feeds the hydrodynamic load to the solid at each time-exchange step. The FE solver computes the solid displacement u, which is then used to determine the new structure of the DPN.

More precisely, the updated set of displacements are used to compute the new position of the solid boundary. The structural computation updates the position of the structural surface. Thus, an updated fluid domain is needed to accommodate the new interface location. We achieved this by performing a re-extraction process for the network. This provides a new value for the node radius $\{r'_i\}$ and volume $\{V'_i\}$, as well as a new throat length $\{l'_{ij}\}$ and radius $\{r'_{ij}\}$. An iterative process is also required at each time step to ensure that the coupled system converges to a steady solution before advancing to the next time step. This is done to reduce the magnitude of errors that could occur during the network re-extraction process. We examine this further in § 3. Another important aspect of the fluid-solid coupling procedure is the hydrodynamic load calculation. The force on the pore body is calculated with the following equation:

$$\boldsymbol{F}_{i} = \int_{\Gamma_{i,f}} P_{i} \boldsymbol{n} \, \mathrm{d}s, \quad \text{on } \Gamma_{i,f}$$
 (2.25)

where F_i is the pressure force applied by the *i*th pore with pore pressure P_i . The boundary of the *i*th pore is $\Gamma_{i,f}$ and n is the unit vector pointing from the centroid of the pore to the nearest solid boundary. Since we are using spherical DPN nodes, we assume the force is the same across the same pore-body node. The fluid load from the pore-body surface along the normal direction is imparted to the solid nodes. One of the central features in this coupling implementation is the exchange of information across the fluid and solid domains. As demonstrated in figure 3(a), the transmission of the fluid load to the solid would require a secondary domain for interfacing both subsystems since the adjoining pore bodies and solid do not match exactly.

2.3.1. Convex hull

In this work, the fluid loads are transmitted to solid nodal points that border an arbitrary volume surrounding the nearest pore body and throat. This initially requires test point values (spatial surface data) generated on the pore network, followed by a sequential neighbourhood search for FE nodal points within a prescribed region of the test point data. Several volumetric shapes could be used to enclose the points (e.g. the

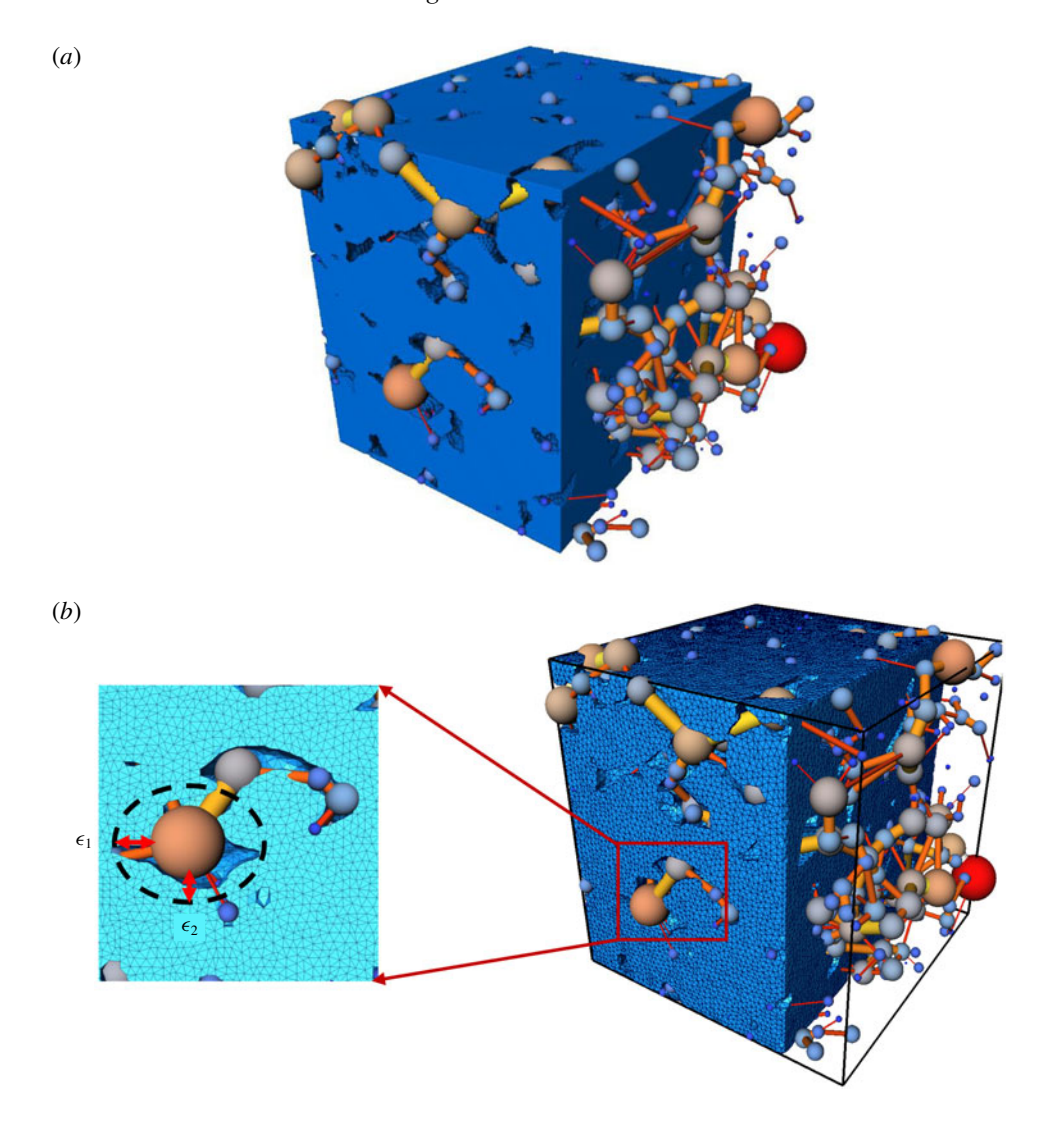


FIGURE 3. Schematic of the superimposed domains (fluid and solid). (a) The voxelized solid phase along with the PN and (b) discretized finite element domain and PN.

smallest cube or sphere). However, we use a convex hull, which is defined as the smallest convex set enclosing the points. The convex hull helps reduce the amount of empty space and saves memory. Calculation of convex hulls is a well-studied problem in computational geometry and this method has diverse applications in other fields, such as cluster analysis, collision detection, image processing, statistics, sphere packing and point location (Barber, Dobkin & Huhdanpaa 1996). It has also been applied in the natural element method (Sukumar, Moran & Belytschko 1998), which relies on Delaunay triangulations in \mathbb{R}^n , computed from convex hull in \mathbb{R}^{n+1} , to construct its interpolants. Convex hull has also been applied for modelling geophysical phenomena and complex FSI problems (Sukumar *et al.* 1998). We define a convex hull as follows: for a set of randomly generated points $\Upsilon^k = \{\gamma_1, \gamma_2, \ldots, \gamma_N\}$ on the *k*th pore in \mathbb{R}^n , the convex hull *C* of the points is expressed mathematically

in the form

$$C = \left\{ \sum_{i=1}^{n} \lambda_i \gamma_i \colon \lambda_i \geqslant 0 \forall i \in \{1, \dots, n\} \land \sum_{i=1}^{n} \lambda_i = 1 \right\}.$$
 (2.26)

Equation (2.26) describes the convex combinations of points in set Υ . For an n-dimensional convex hull set of nodal points, we apply the Quickhull (known as Qhull) algorithm developed by Barber et al. (1996) to calculate the convex hull of sets of the multidimensional points of that hull. The hull is created based on random points (test points) generated on the surface of pores. Now for such a set of points, if a distinctive portion of the finite element nodal points ($n = \{n_1, n_2, \ldots, n_M\}$) and Υ are found within the same space, they are labelled unity, while points outside are labelled zero. This process is graphically shown in figure 4. The forces F_i are then transmitted to nodes labelled unity while others outside this space, labelled zero, are left out.

Thus, at each time step, the coupling algorithm proposed in this work has the following sequence of operations:

Algorithm 1 Pseudo-code for coupling operation.

```
1: Initialize variables: F_i = 0, t = 0, v_*^0 = v^0, u_*^0 = u^0, k = 0, n = 0
  2: Apply boundary conditions to the solid phase, u, \overline{T}
  3: Solve FE
              u^{n+1}, v^{n+1}, K^{int}
  4.
              TDG, \boldsymbol{v}_*^{n+1} = \overline{\boldsymbol{u}}_1^l, \boldsymbol{u}_*^{n+1} = \boldsymbol{u}_*^n + \Delta t [(1 - \alpha^*) \overline{\boldsymbol{u}}_0^l + \alpha^* \overline{\boldsymbol{u}}_1^l]
Update quantities, \boldsymbol{u}^{n+1} = \boldsymbol{u}_*^{n+1}, \boldsymbol{v}^{n+1} = \boldsymbol{v}_*^{n+1}
  5:
  7: Extract DPN: \{V_i\}, \{l_{ij}\}, \{r_{ij}\}.
  8: Initialize fluid forces: F_i = 0.
  9: Set the number of precoupling iterations→Iter.
10: Solve (2.8).
11:
          while l < Iter
12:
              P_i, t, P_{max}
              Update position of the solid
13:
14:
              Voxelize solid domain
              Perform re-extraction of the network: \{V_i^*\}, \{l_{ii}^*\}, \{r_{ii}^*\}.
15:
              Determine average PSD
16:
                     if E_a(\overline{X}_p) > tol
17:
18:
                      l = l + 1, else terminate
19:
          end while loop
20: for time, t
          Find F_i^{t+1} using (2.25).
21:
              (a) identify n \in n in convex hull set \Upsilon^k
22:
             (b) \boldsymbol{F}_{i}^{t+1} = \boldsymbol{f}_{ext}
23:
              Repeat step 3
24:
25:
          Update t = t + \Delta t
26: end for loop
```

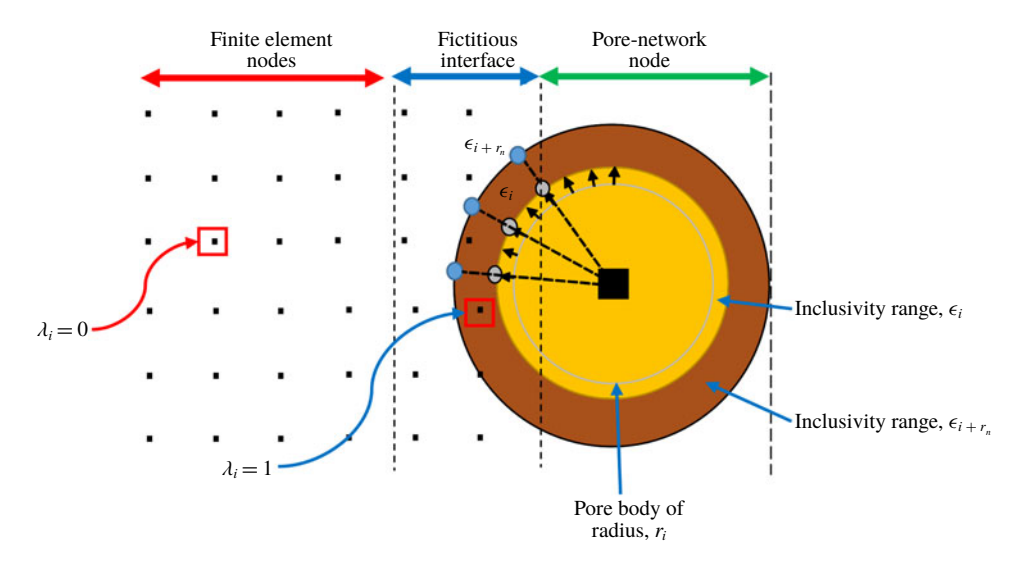


FIGURE 4. Test points used for convex hulling. The hydrodynamic load is transferred to the solid mesh node points by linear interpolation of node points within the convex hull. Here, ϵ_{i+r_n} represents the enlarged hull volume to include more points for interpolation. Points enclosed within ϵ_{i+r_n} are labelled as one. Points outside are zero.

3. Numerical results

The coupled technique was used to simulate the drainage of water by oil in a water-wet system in a Berea sandstone sample. The deformation of the solid was investigated during the drainage process. The DPN domain was extracted from the sandstone image such that the image in binary was defined by

$$\mathcal{I} = \begin{cases} 1, & Z \in \text{ pore} \\ 0, & Z \in \text{ solid,} \end{cases}$$
 (3.1)

where 1 represents the pores and 0 the solid. Here, Z denotes an arbitrary voxel in the binarized image. Extraction was achieved using the maximal ball algorithm (Dong & Blunt 2009). Tetrahedral meshes were generated directly from the image for the solid domain. The domain size (L_x, L_y, L_z) is (0.641, 0.641, 0.641) mm. Absolute permeability and void fraction are 210mD and 18.82%, respectively. Details of the simulation parameters can be found in table 2.

3.1. Boundary conditions

As mentioned earlier, DPN models are well suited for multiphase flow simulation. In this study, therefore, we considered a two-phase flow model, containing oil and water. We carried out drainage for a water-wet system (water is the wetting fluid and oil is the non-wetting fluid). Both fluids are incompressible and immiscible. The wetting phase has a dynamic viscosity of 1 cP and the non-wetting phase has a dynamic viscosity of 10 cP. Dynamic pore network simulation began with an injection of water across the network with a constant flow rate of 1.25×10^{-13} m³ s⁻¹ at the inlet. Simulation continued until after the length of the injection time was attained, which in this case was 20 s. The contact angle was set at 0° at the inlet because only water was present at the start of the simulation and oil had not yet begun to displace water.

Parameters	Value
Number of FE nodes	11 976
Number of FE elements	56 559
Elastic modulus	$20 \times 10^9 \text{ Pa}$
Poisson ratio	0.28
Number of DPN pore nodes	240
Inlet flow rate	$1.25 \times 10^{-13} \text{ m}^3 \text{ s}^{-1}$
Injection time	20 s
Domain size	0.641, 0.641, 0.641 mm
Void fraction (i.e. porosity)	18.82 %

TABLE 2. Properties used for the coupled simulation.

3.2. Results

At low flow rates, the capillary forces are more dominant than the viscous forces. This is governed by capillary number $Ca = u_f \mu/\gamma_{sf}$, where u_f is the fluid velocity, μ is the dynamic viscosity and γ_{sf} is the interfacial tension. The viscous pressure drop (ΔP_{μ}) can play a major role when the flow rate is high when the characteristic length L_x of the representative element volume is large, or in near-miscible displacements with low interfacial tension. Capillary pressure scales as $P_c = 2\gamma_{sf}/r_c \sim \gamma_{sf}\sqrt{P_{\mu}/K}$, where r_c is the mean radius of interfacial curvature. The viscous pressure drop scales as $\Delta P_{\mu} = q_f \mu L_x/K$, where K is the effective rock permeability. Therefore, the capillary pressure is not related to flow rate or L_x . When the ratio of viscous pressure drop to capillary pressure is high, macroscopic flow properties (e.g. relative permeability) can be a function of flow rate, leading to a Darcy law scenario in which flow rate nonlinearly depends on the pressure gradient. For this work, however, we only consider low flow rates that correspond to a capillary-dominated flow regime.

Figure 5 illustrates the drainage sequence at DPN simulation times. It can be observed that water sweeps the oil phase continually from the pore space by a piston-like displacement. Over time, more residing fluid was swept through the outlet. As the wetting phase was being displaced, we kept track of the hydrodynamic or pressure forces that are to be exchanged across the fictitious fluid–solid interface.

The deformation of the solid induced by fluid pressure is observed in figures 6 and 7. It can be seen that the forces at the throats are very small compared to those at the pores; thus, the forces at the throats can be ignored.

At the final time of the simulation, in figure 7(d), there is a greater distribution of pores with higher pressure forces than those in the earlier drainage sequence, because most of the pores have been invaded by the non-wetting phase. The deformation resulting from the local displacement of the wetting phase fluid is illustrated in figure 7(e-h), for which the maximum $(5.67 \times 10^{-5} \, \mu \text{m})$ occurs at the end of the injection process.

We applied several random distributions to select the test points on the pore surface. Each test point was selected randomly from the interval $[-r_{i,j}, r_{i,j}]$. In this work, we considered data from 100 to 1000 random test points on each spherical pore body surface. We then conducted a sensitivity analysis for the optimum number of test points to be used for the simulations. Figure 8, for example, shows how the capillary pressure solution is affected by varying the number of test points. It can be observed in the earlier part of the displacement process (from the right-hand side) that the capillary pressure (P_c) values are more sensitive to the number of

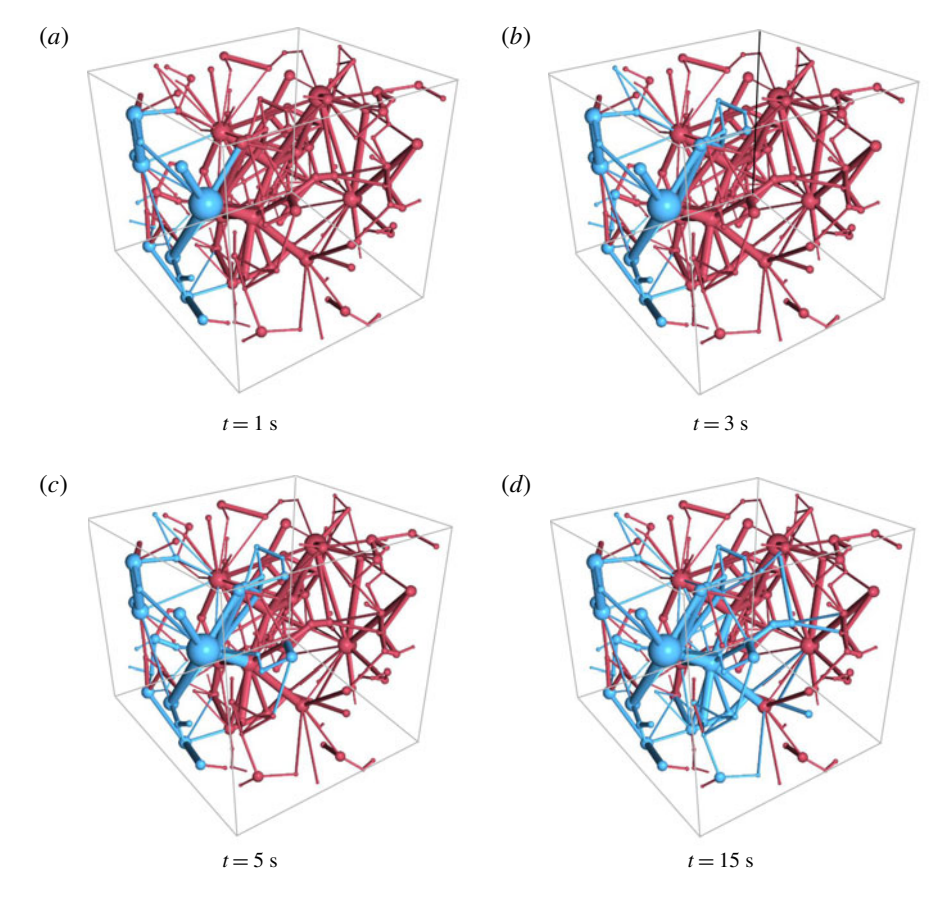


FIGURE 5. Drainage evolution in time for a water-wet system (oil is blue and water is red).

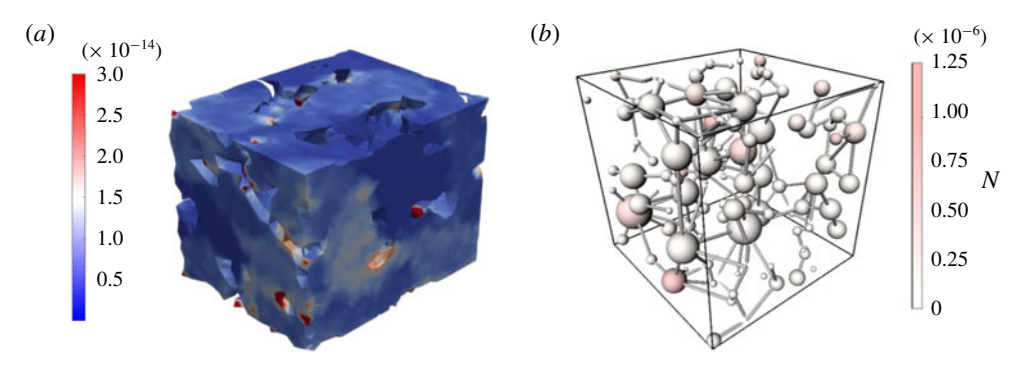


FIGURE 6. Solid deformed as a result of fluids residing in the pores at different pore pressures.

test points used; using more points lowers P_c values by approximately 13.5 kPa. As water saturation decreases, this value becomes less dependent on the number of test points. Based on our preliminary results, 800 test points proved to be sufficient for

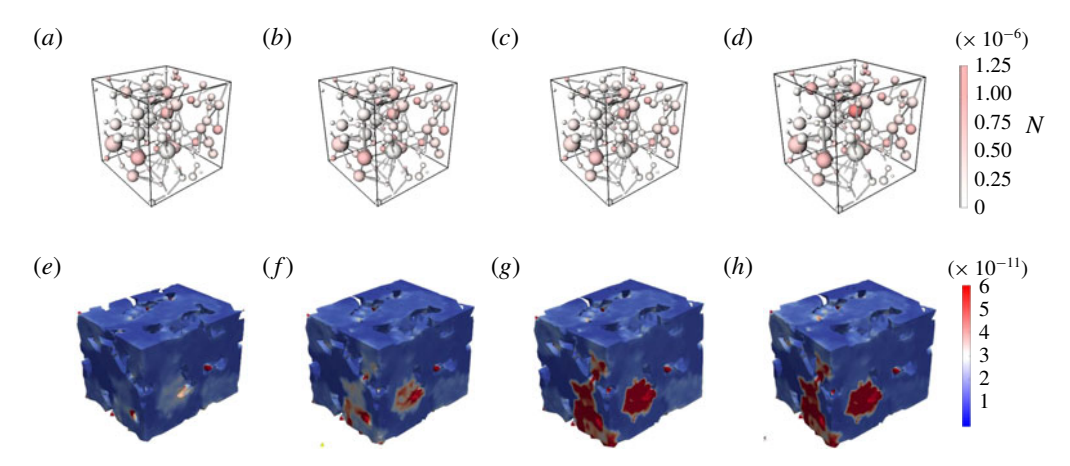


FIGURE 7. Hydrodynamic forces and the corresponding deformation induced by nodal pressure in the network at times 1 s, 3 s, 5 s and 15 s, respectively.

our simulation. Another important parameter we considered in the coupling procedure is the tolerance/range of inclusivity. The apparent gap between both domains requires that the hull of pore body spatial points be enlarged to accommodate more FE nodal points, as seen in figure 4. This is achieved by defining a tolerance that can be interpreted as the range of FE points, away from the convex hull, which could still be regarded as an interpolation point. The tolerance and range of inclusivity are given as

$$\epsilon_i = \eta \frac{\sum_i \gamma_i}{N}, \quad \epsilon_{i+r_n} = r_n + \eta \frac{\sum_i \gamma_i}{N},$$
(3.2)

where ϵ_i and ϵ_{i+r_n} are ranges of inclusivity, η is a constant that depends on the size of the pore body radius r_i and N is the total number of test points used for each pore body. Here, r_n is a value that varies with r_i where $r_n < r_i$. For all simulations, we examined the sensitivity of each FE node point n_k , with respect to $\|\epsilon_{i+r_n}\|$.

We also examined the effect of inflow volumetric rate on deformation in a four-case scenario while maintaining pre-existing boundary conditions. The first case, case A, had a flow rate of 1.25×10^{-13} m³ s⁻¹, while the base case (case B) had a flow rate of 2.5×10^{-13} m³ s⁻¹. The flow rates of cases C and D were 5.0×10^{-11} m³ s⁻¹ and 5.0×10^{-10} m³ s⁻¹, respectively. Flow rates were increased and the subsequent deformation and von Mises stress were computed. The results are shown in figures 9(a) and 9(b), respectively. The deformation and stress increased monotonically for the flow rate up to a critical point, slightly below 1.0×10^{-10} m³ s⁻¹. Thereafter, the solid deformed more significantly for all cases.

A precoupling step was required, as indicated in algorithm 1, to ensure that the coupled system would converge to a steady solution before advancing to the next time step. The number of iterations would depend on the nature of the imaged data. The coordination number, which is the average number of pore bodies connected to a specific pore, could be affected based on the nature of the image from which the network is derived. Consequently, the stochastic nature of the maximal ball algorithm would generate inconsistent values for the maximum and minimum pore body and throat sizes for each re-extraction. Hence, we define a function $E_a(\overline{X}_p)$ which quantifies the error between each subiteration before the start of the transient

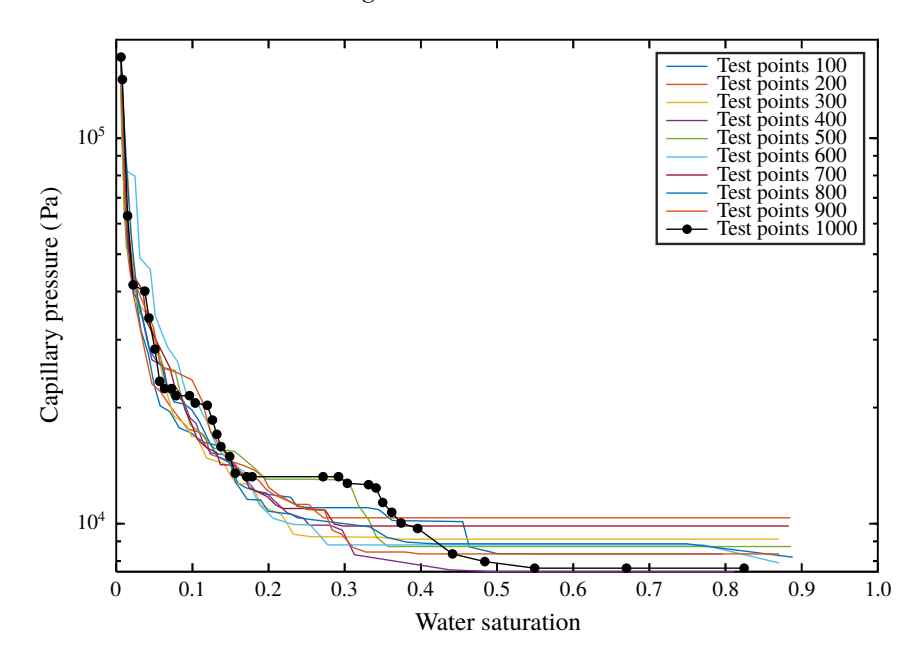


FIGURE 8. Effects of the number of test points on the capillary pressure solution for drainage in the water-wet system.

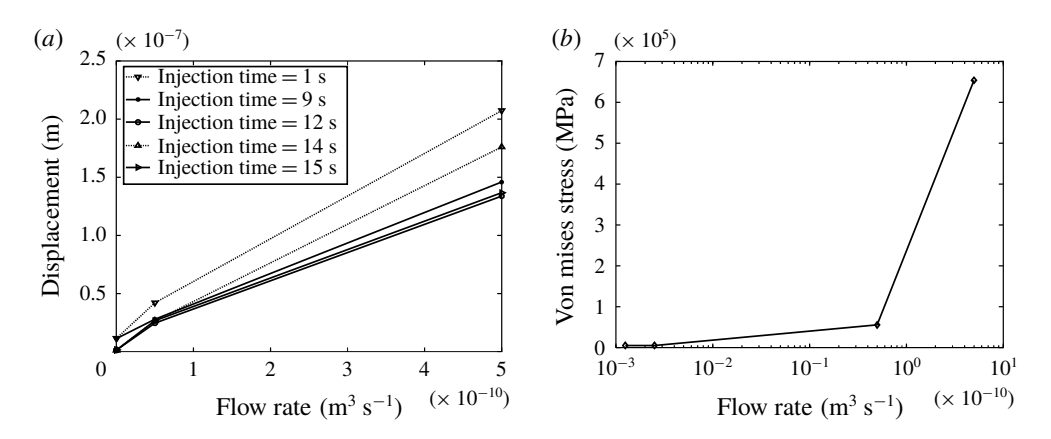


FIGURE 9. Evolution of (a) solid deformation and (b) the von Mises stress at different flow rates.

coupling procedure. Each iteration p signifies p number of re-extractions performed. This error is defined by the following equation:

$$E_a(\overline{X}_p) = \frac{|\overline{X}(p) - \overline{X}(p+1)|}{\overline{X}(p)},$$
(3.3)

where $\overline{X}(p)$ is the average value of the pore size at iteration p. This error allows us to estimate the accuracy of the extraction code, especially when boundary conditions are applied to the solid. In all of the proposed computational tests, the coupled system

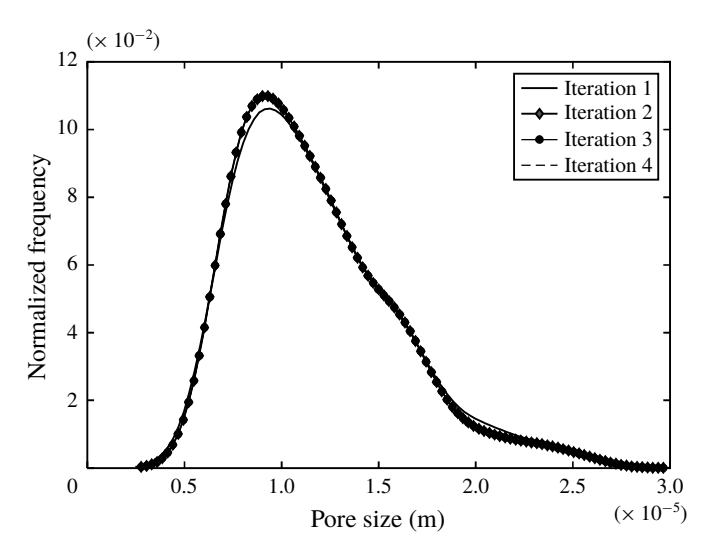


FIGURE 10. Convergence of pore network extractions.

advances if $E_a(\overline{X}_p)$ is smaller than a prescribed tolerance value. From figure 10, it is observed that the network extraction converged after four iterations.

3.3. The effect of boundary conditions during drainage

Several boundary loads were applied on the solid in the axial direction to investigate how such prescribed values affect flow properties. The absolute permeability and pore-size distribution were tracked as the simulation progressed. Figure 12(a) indicates the boundary conditions applied in this work. By applying a constant strain rate $\dot{\varepsilon}(=\Delta z/(L_z\Delta t))$ at boundary $\mathcal{B}(x_2)=L$, we monitored the deformation. A fixed constraint (zero displacement boundary condition) at boundary $\mathcal{B}(x_2)=0$ was applied at the opposite boundary; rollers were used at the other boundaries to prevent the collapse of the solid normal to that boundary. The solid boundary loads were only applied at the beginning of the simulation, while the hydrodynamic forces were coupled at each subsequent iteration.

Plots of solid displacement during loading are represented in figure 11. These results are taken at the same time corresponding to vertical strains of 0.00056 and 0.00160. The pore-size distribution (PSD) evolution is shown in figure 13 at different coupling times ranging from 1 s to 20 s. At these times, the results illustrate a shift in the PSD to the left, indicating a reduction in pore-size and the closures of some pores. There is also a vertical shift upwards, implying an increase in the number of smaller-sized pores. However, at much higher strain rate values, the distribution shifts downwards and the rest of the pore sizes are spread primarily to the right (with some to the left), indicating constriction as well as lateral dilation of some pores due to stress. The network also becomes distorted at equilibrium points as higher strain rate values are applied. Figure 14 shows a snapshot of the physical structure of the network after the deformation. The pore pressure also increases as the strain increases, as seen in figure 12(b). Another important property that we monitored during the deformation process was absolute permeability. Figure 15 shows the effect of the loading on absolute permeability. It can be observed that absolute permeability

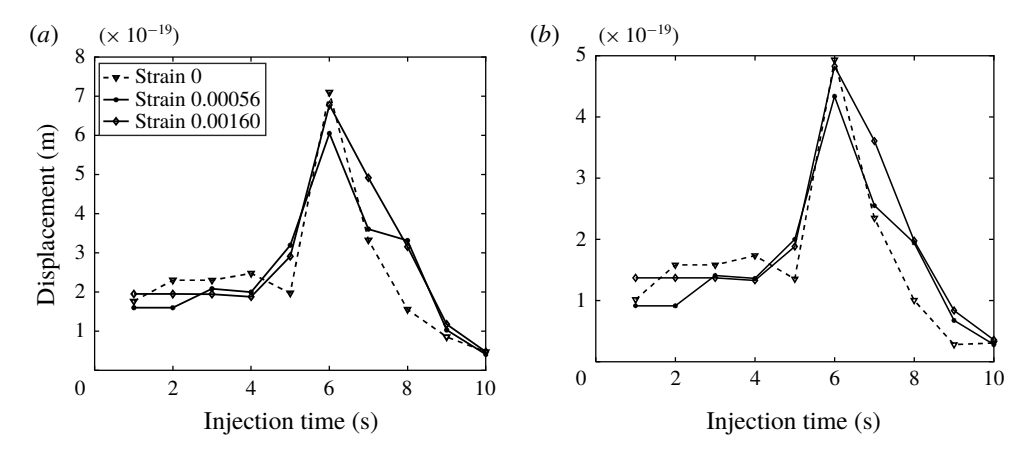


FIGURE 11. Solid deformation resulting from strain rates applied. Results are shown for two FE nodes, with 800 test points and $\epsilon_{i+r_n} = 8 \times 10^{-5}$.

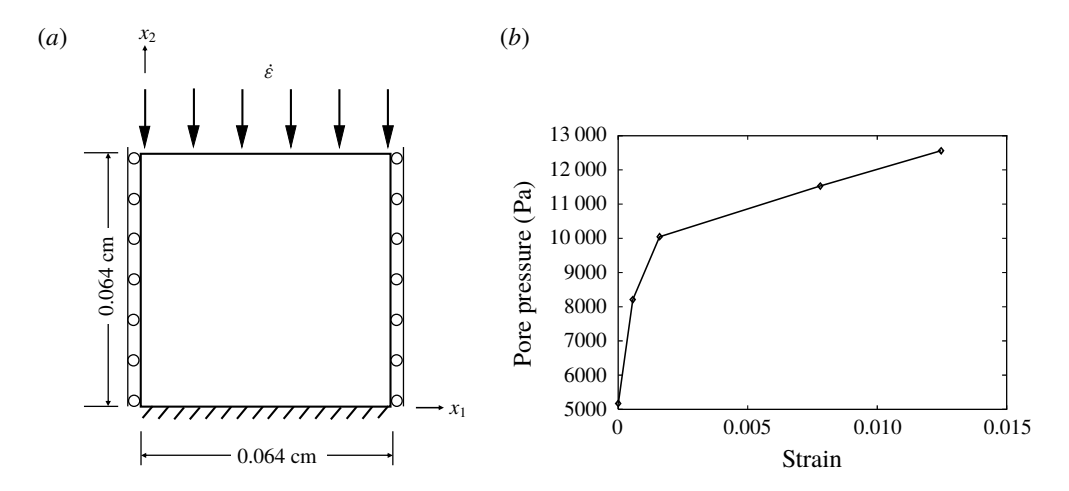


FIGURE 12. (a) Solid boundary conditions used in microscale tests. (b) Pore pressure change.

decreased as more load was applied. Furthermore, due to rearrangements of the pore network, precoupling iterations were carried out as shown in figure 10. It is apparent that the solution converged after four iterations.

3.4. Verification of results

We tested the results of the coupled FE-DPN* pore-scale model for accuracy. A coupled finite volume system was used as the basis for the comparison (Fagbemi, Tahmasebi & Piri 2020). The system constitutes a strongly coupled partitioned solver whose meshes are unstructured, independent and conformed at the interface. The hydrodynamic load is transmitted via face interpolation while the displacement is exchanged using vertex interpolation. The initial computational domain is an undeformed porous medium of size 10³ mm. The sample geometry, and the preprocessing steps, are shown in figure 16. The drainage sequence began with the wetting phase occupying the entire computational fluid domain. Then, based

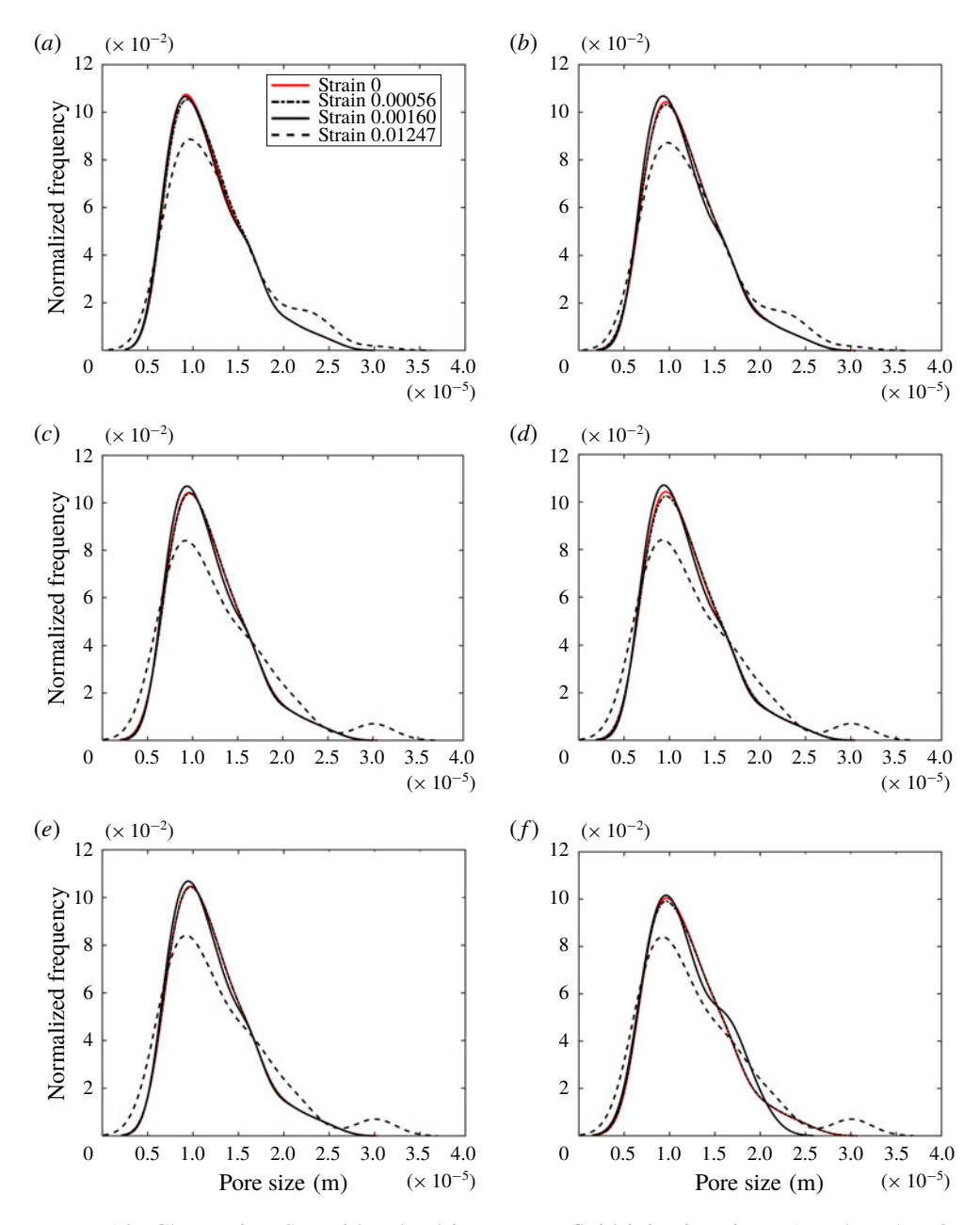


FIGURE 13. Change in PSD with a load increase at fluid injection times 1 s, 4 s, 5 s, 8 s, 10 s and 14 s. There is an apparent shift to the left of the original plot when the solid is compacted in the axial direction, indicating a reduction in the pore radii. At a strain value of 0.01247, there is constriction as well as lateral dilation of some pores due to stress.

on prescribed initial secondary fluid saturation, the non-wetting phase displaces the wetting phase.

Similar flow rates were used, while a fixed pressure value boundary condition of zero was used at the outlet. No-slip boundary conditions were applied at the walls.

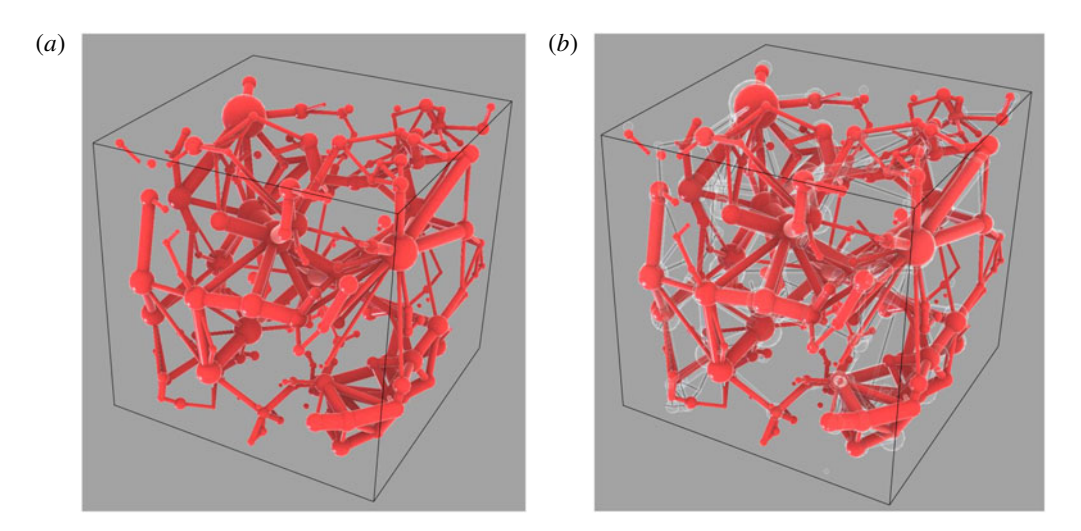


FIGURE 14. The network (a) before deformation and (b) after deformation. The differences between (a) and (b) are noted by white colouring in (b).

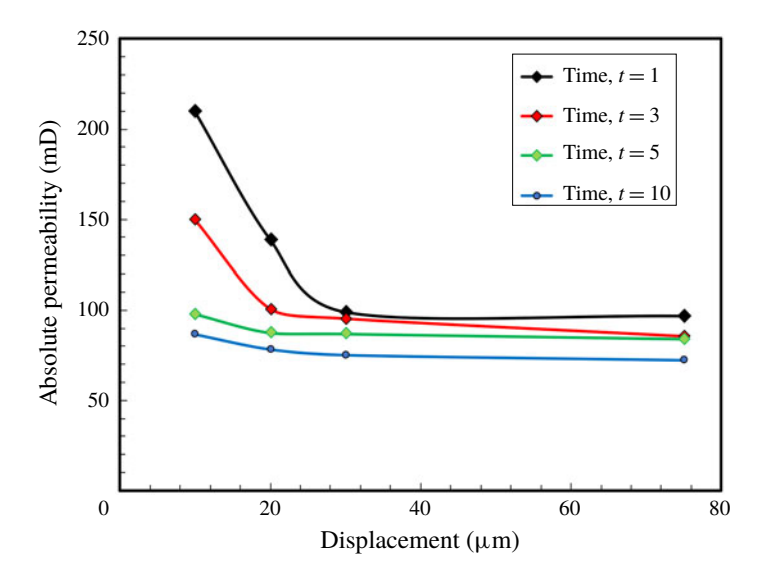


FIGURE 15. Absolute permeability evolution at different times.

Plots of deformation at selected mesh nodes, at the third time step from the last time $||d_{T-3}||$, are compared for both solvers. As illustrated in figure 17, the results are in good agreement with those from the FE-DPN* model. The deformations for both solvers induced by fluid injection at lower flow rates are very similar. However, at higher flow rates, we begin to see a separation of values.

4. Conclusion

We presented a new multimethod approach for studying fluid and solid interaction problems at the pore-scale. This approach drastically reduces the time required for computing results of the coupled solid and fluid analysis. We represented the pore

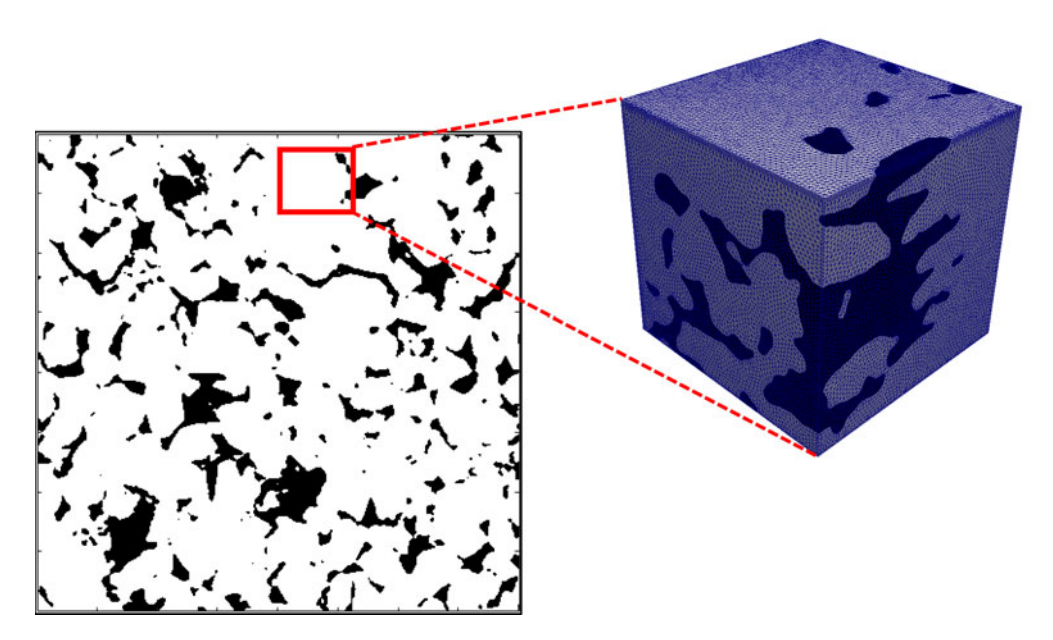


FIGURE 16. The FV geometry, similar to the coupled model used in this work, was obtained using micro-CT imaging technology. To effectively study the effects of external stresses and fluid forces on the sample at the pore-scale, high-porosity Berea sandstone was used. The Berea image was initially filtered to improve the signal-to-noise ratio and then subsequently segmented into binary data, where each domain is represented by 0 or 1. The rock image sample has a pore volume fraction of 21.174 %. The original voxel size of the sample was 1000^3 , which was later resized to 120^3 for the simulation.

structure as a network of spheres and cylinders for each pore and throat in space, respectively. The solid was represented using real segmented images generated by X-ray micro computed tomography (micro-CT) technology. The computational domain comprised a segregated two-way coupled system composed of a solid subdomain, having unstructured meshes whose nonlinear response was investigated using FEM; and a fluid subdomain whose flow characteristics was modelled using dynamic pore network method. Due to the meshless nature of the DPN and incongruity of the solid surface, hydrodynamic load transmission to the FE solver is a non-trivial task. In this work, continuity of stress was achieved by interpolation of fluid forces directly across a fictitious boundary. Solid nodal points and selected tested points on the surface of the pore bodies were interpolated within a convex hull of points based on a defined range of inclusivity. The deformation of the solid, which results in a rearrangement of its structure, required that the pore network be updated regularly during the simulation to track the deformation of the solid. The pore network was hence re-extracted at each time interval. Curtailing the host of potential errors from such a stochastic process required the implementation of several coupling subiterations which ensured that the average pore-size distribution was uniform at every time step. From our results, these errors were very minimal, indicating the potential of this technique for studying more complex interactions of fluid in complex solid media. We applied the coupled model for investigating solid deformation during the drainage process for capillary-dominated flow regimes. The effect of boundary conditions prescribed in the solid subdomain on the pore size distribution and absolute permeability were

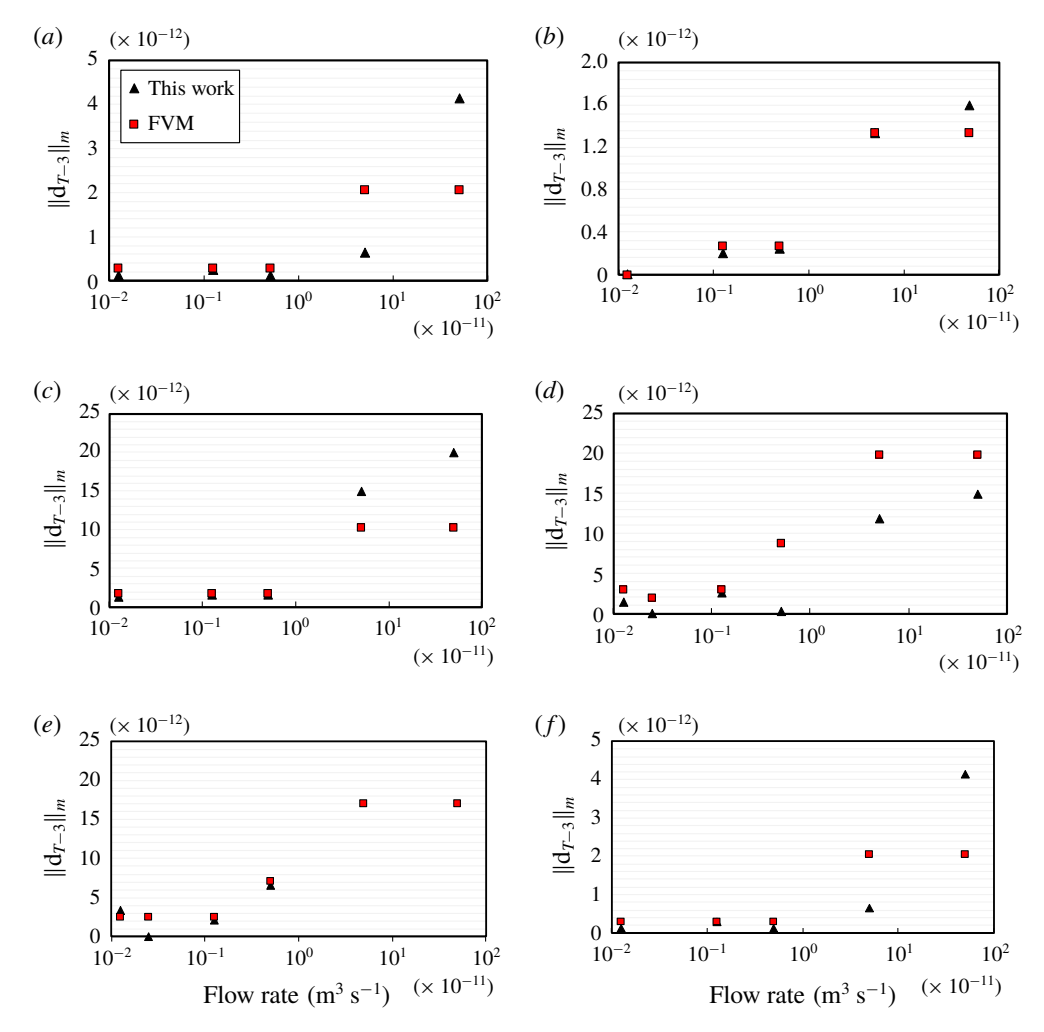


FIGURE 17. Verification of results for solid deformation from the finite volume model (FVM) and this work for selected nodal points, at the third time step from the last time $\|d_{T-3}\|$.

equally studied. Results from such computational experiments were then compared with those from a coupled finite volume solver, showing good agreement. One of the main applications of this approach is for modelling of deformation in large-scale problems for which direct numerical simulations and lattice Boltzmann methods for coupled systems are computationally expensive.

Acknowledgements

We would like to thank the University of Wyoming for financial support for this research. This study was partially supported by NSF (grant #CMMI-2000966), NIH (grant #P20GM103432) and NASA (grant #80NSSC19M0061).

Declaration of interests

The authors report no conflict of interest.

REFERENCES

- AKER, E., JØRGEN MÅLØY, K., HANSEN, A. & BATROUNI, G. G. 1998 A two-dimensional network simulator for two-phase flow in porous media. *Trans. Porous Med.* 32, 163–186.
- ALVAREZ, J. B. 2017 Interaction of multiphase fluids and solids: theory, algorithms and applications. PhD thesis, University of Coruna.
- BARBER, C. B., DOBKIN, D. P. & HUHDANPAA, H. 1996 The quickhull algorithm for convex hulls. *ACM Trans. Math. Softw.* **22**, 469–483.
- BATHE, K. J. & ZHANG, H. 2004 Finite element developments for general fluid flows with structural interactions. *Intl J. Numer. Meth. Engng* **60**, 213–232.
- BATHE, K. J., ZHANG, H. & JI, S. 1999 Finite element analysis of fluid flows fully coupled with structural interactions. *Comput. Struct.* 72, 1–16.
- BIJELJIC, B. & BLUNT, M. J. 2007 Pore-scale modeling of transverse dispersion in porous media. Water Resour. Res. 43, W12S11.
- BLUNT, M. 1995 Pore-level model of wetting. Phys. Rev. E 52, 6387-6403.
- BRYANT, S. & BLUNT, M. 1992 Prediction of relative permeability in simple porous media. *Phys. Rev.* A **46**, 2004–2011.
- BUENO, J. & GOMEZ, H. 2016 Liquid-vapor transformations with surfactants. Phase-field model and isogeometric analysis. *J. Comput. Phys.* **321**, 797–818.
- CAMPBELL, R. L. 2010 Fluid-structure interaction and inverse design simulations for flexible turbomachinery. PhD thesis, Pennsylvania State University.
- CELIA, M. A., REEVES, P. C. & FERRAND, L. A. 1995 Recent advances in pore scale models for multiphase flow in porous media. *Rev. Geophys.* 33, 1049–1057.
- CHEN, M., YORTSOS, Y. C. & ROSSEN, W. R. 2005 Insights on foam generation in porous media from pore-network studies. *Colloids Surf.* A **256**, 181–189.
- DE ROSIS, A., FALCUCCI, G., PORFIRI, M., UBERTINI, F. & UBERTINI, S. 2014 Hydroelastic analysis of hull slamming coupling lattice Boltzmann and finite element methods. *Comput. Struct.* 138, 24–35.
- DENOËL, V. & DETOURNAY, E. 2011 Eulerian formulation of constrained elastica. *Intl J. Solids Struct.* **48**, 625–636.
- DONG, H. & BLUNT, M. J. 2009 Pore-network extraction from micro-computerized-tomography images. *Phys. Rev.* E **80**, 036307.
- FAGBEMI, S., TAHMASEBI, P. & PIRI, M. 2020 Numerical modeling of strongly coupled microscale multiphase flow and solid deformation. *Intl J. Numer. Anal. Meth. Geomech.* 44 (2), 161–182.
 FATT, I. 1956 The network model of porous media. *Trans. AIME* 207, 144–181.
- FIGUS, C., BRAY, Y. L., BORIES, S. & PRAT, M. 1999 Heat and mass transfer with phase change in aporous structure partially heated: continuum model and pore network simulations. *Intl J. Heat Mass Transfer.* **42**, 2557–2569.
- GELLER, S., KOLLMANNSBERGER, S., BETTAH, E. E., KRAFCZYK, M., SCHOLZ, D., DUSTER, A. & RANK, E. 2010 An explicit model for three-dimensional fluid-structure interaction using LBM and p-FEM. In *Fluid-Structure Interaction II* (ed. H.-J. Bungartz, M. Mehl & M. Schäfer), Lecture Notes in Computational Science and Engineering, pp. 285–325. Springer.
- GOMES, J. P. & LIENHART, H. 2006 Experimental study on a fluid-structure interaction reference test case. In *Fluid-Structure Interaction* (ed. H.-J. Bungartz & M. Schäfer), Lecture Notes in Computational Science and Engineering, pp. 356–370. Springer.
- HAN, Y. P. A. C. & CUNDALL, P. A. 2012 LBM-DEM modeling of fluid-solid interaction in porous media. *Intl J. Numer. Anal. Methods Geomech.* 37, 1391–1407.
- JOEKAR-NIASAR, V. & HASSANIZADEH, S. M. 2012 Analysis of fundamentals of two-phase flow in porous media using dynamic pore-network models: a review. Crit. Rev. Environ. Sci. Technol. 42, 1895–1976.
- KHARABAF, H. & YORTSOS, Y. C. 1998 A pore-network model for foam formation and propagation in porous media. SPE J. 3, 42–53.
- KOLLMANNSBERGER, S., GELLER, S., DUSTER, A., TOLKE, J., SORGER, C., KRAFCZYK, M. & RANK, E. 2009 Fixed-grid fluid-structure interaction in two dimensions based on a partitioned lattice Boltzmann and p-FEM approach. *Intl J. Numer. Meth. Engng* **79**, 817–845.

- LI, J., MCDOUGALL, S. R. & SORBIE, K. S. 2017 Dynamic pore-scale network model (PNM) of water imbibition in porous media. *Adv. Water Resour.* **107**, 191–211.
- MANCUSO, M. & UBERTINI, F. 2003 An efficient integration procedure for linear dynamics based on a time discontinuous Galerkin formulation. *Comput. Mech.* 32, 154–168.
- MANCUSO, MASSIMO & UBERTINI, F. 2002 The Nørsett time integration methodology for finite element transient analysis. *Comput. Meth. Appl. Mech. Engng* 191, 3297–3327.
- MUNSCH, M. & BREUER, M. 2010 Numerical simulation of fluid-structure interaction using eddyresolving schemes. In *Fluid-Structure Interaction* (ed. H.-J. Bungartz, M. Mehl & M. Schäfer), Lecture Notes in Computational Science and Engineering, pp. 221–253. Springer.
- NOELS, L. & RADOVITZKY, R. 2008 An explicit discontinuous Galerkin method for non-linear solid dynamics: formulation, parallel implementation and scalability properties. *Intl J. Numer. Meth. Engng* **74**, 1393–1420.
- OREN, P.-E., BAKKE, S. & ARNTZEN, O. J. 1998 Extending predictive capabilities to network models. SPE J. 3, 324–336.
- Pereira, G. G., Pinczewski, W. V, Chan, D. Y. C., Paterson, L. & Oren, E. E. 1996 Porescale network model for drainage-dominated three-phase flow in porous media. In *Transport in Porous Media*, vol. 24. Kluwer.
- RUGONYI, S. & BATHE, K. J. 2001 On finite element analysis of fluid flows coupled with structural interaction. *Comput. Model. Engng Sci.* **2**, 195–212.
- SATHE, S. & TEZDUYAR, T. E. 2008 Modeling of fluid-structure interactions with the space-time finite elements: contact problems. *Comput. Mech.* **43**, 51.
- SUKUMAR, N., MORAN, B. & BELYTSCHKO, T. 1998 The natural element method in solid mechanics. *Intl J. Numer. Meth. Engng* 43, 839–887.
- TAHMASEBI, P. & KAMRAVA, S. 2019 A pore-scale mathematical modeling of fluid-particle interactions: thermo-hydro-mechanical coupling. *Intl J. Greenh. Gas Control* **83**, 245–255.
- TUREK, S., HRON, J., RAZZAQ, M., WOBKER, H. & SCHÄFER, M. 2010 Numerical benchmarking of fluid–structure interaction: a comparison of different discretization and solution approaches. In *Fluid–Structure Interaction II* (ed. H.-J. Bungartz, M. Mehl & M. Schäfer), pp. 413–424. Springer.
- TUREK, S. & HRON, J. 2006 Proposal for numerical benchmarking of fluid–structure interaction between an elastic object and laminar incompressible flow. In *Fluid–Structure Interaction*, pp. 371–385. Springer.
- VIERENDEELS, J., LANOYE, L., DEGROOTE, J. & VERDONCK, P. 2007 Implicit coupling of partitioned fluid-structure interaction problems with reduced order models. *Comput. Struct.* **85**, 970–976.
- ZHANG, X. & TAHMASEBI, P. 2018 Micromechanical evaluation of rock and fluid interactions. *Intl J. Greenh. Gas Control* **76**, 266–277.
- ZHU, Q. J., HE, Y. F. & YIN, Y. 2014 Finite element analysis of deformation mechanism for porous materials under fluid–solid interaction. *Mater. Res. Innov.* 18, 22–27.
- ZHU, W. & WONG, T.-F. 1996 Permeability reduction in a dilating rock: network modeling of damage and tortuosity. *Geophys. Res. Lett.* 23, 3099–3102.
- ZIENKIEWICZ, O. C., TAYLOR, R. L. & TAYLOR, R. L. 2000 The Finite Element Method: Solid Mechanics, vol. 2. Butterworth-Heinemann.